Research Square

Preprints are preliminary reports that have not undergone peer review.
They should not be considered conclusive, used to inform clinical practice,
or referenced by the media as validated information.

Zeaxanthin couples intracellular Ca^{2+} homeostasis to CAMKK2/AMPK-dependent mitochondrial recovery in senescent muscle

Tianyu Liu
Jilin Agricultural University
Zhina Hao
Jilin Agricultural University
Yuan Chen
Jilin Agricultural University
Wanying Li
Jilin Agricultural University
Chunlei Liu
Jilin Agricultural University
Xiuying Xu
Jilin Agricultural University
Jingsheng Liu
Jilin Agricultural University
Meihong Liu
liumh@jlau.edu.cn
Jilin Agricultural University
Guangquan Ren
Jilin Agricultural University

Article

Keywords: Zeaxanthin, Senescent muscle, Intracellular Ca2+ homeostasis, Mitochondrial recovery

Posted Date: November 20th, 2026

DOI: https://doi.org/10.21203/rs.3.rs-11183610/v1

License: This work is licensed under a Creative Commons Attribution 4.0 International License.
Read Full License

Additional Declarations: No competing interests reported.

Abstract

Age-related loss of skeletal muscle is tightly linked to mitochondrial failure, disrupted calcium handling and impaired myogenic maintenance, but strategies that coordinate these processes remain limited. Here we show that zeaxanthin protects against sarcopenia-like muscle atrophy in accelerated-aging and cellular-senescence models. In D-galactose-treated mice, 12 weeks of zeaxanthin preserved dystrophin organization, sarcomeric architecture and mitochondrial ultrastructure, and restored markers of mitochondrial fusion, mitophagy and AMPK-associated quality control. In C2-ceramide-induced C2C12 myotubes, zeaxanthin reduced senescence-associated β-galactosidase activity, maintained myotube morphology, restored mitochondrial content and shifted myogenic and atrophy-related markers toward a less degenerative state. Mechanistically, zeaxanthin stabilized intracellular Ca^{2+} distribution across the endoplasmic reticulum, cytosol and mitochondria, reduced pathological mitochondria-associated endoplasmic reticulum membrane coupling and limited mitochondrial Ca^{2+} overload. These changes were accompanied by recovery of mitochondrial membrane potential, respiratory capacity and ATP production, and by activation of the CAMKK2/AMPK metabolic axis; CAMKK2 inhibition blunted these bioenergetic and signalling benefits. Thus, zeaxanthin links Ca^{2+}-mitochondria-associated ER membrane homeostasis to CAMKK2/AMPK-dependent mitochondrial recovery in preclinical models of sarcopenia-like muscle degeneration.

1. Introduction

Ageing progressively erodes skeletal muscle mass, strength and metabolic flexibility, increasing frailty and loss of independence (Larsson et al., 2019). Mitochondria lie at the convergence of these changes because they match ATP supply to contraction while coordinating redox balance, proteostasis and organelle turnover. Human multi-omic profiling now shows that older muscle loses programmes linked to cellular respiration and energy metabolism, whereas sustained physical training preserves a substantial fraction of this molecular signature (Janssens et al., 2026). Genetic evidence further connects mitochondrial maintenance to Ca^{2+} handling: loss of chaperone-mediated autophagy in skeletal muscle alters the mitochondrial proteome, disrupts sarcoplasmic/endoplasmic reticulum Ca^{2+}-ATPase-dependent Ca^{2+} storage and produces progressive myopathy, while restoration of this pathway partly improves ageing muscle phenotypes(Santiago-Fernández et al., 2025). Ca^{2+} links contractile demand to mitochondrial adaptation, yet its disruption in ageing muscle is not uniformly a state of deficiency. Partial separation of mitochondria from contractile Ca^{2+} release sites in old muscle is associated with lower stimulation-evoked mitochondrial Ca^{2+} ($mtCa^{2+}$) uptake and poorer matching of energy supply to contraction(Pietrangelo et al., 2015). Consistent with this deficit, analyses of human muscle biopsies, patient-derived myotubes and preclinical models identified age-related loss of mitochondrial calcium uniporter regulator 1 and impaired $mtCa^{2+}$ uptake (Gherardi et al., 2025). Conversely, naturally aged mice and mice lacking thyroid hormone receptorα in skeletal muscle show increased inositol 1,4,5-trisphosphate receptor 1 expression, greater endoplasmic reticulum-

mitochondrial association and mtCa^{2+} overload(Shi et al., 2026). Insufficient activity-evoked uptake and excessive chronic organelle transfer can therefore emerge in different ageing contexts. Restoring the distribution of Ca^{2+} among intracellular compartments, rather than indiscriminately blocking or increasing mitochondrial entry, may offer a more useful therapeutic principle.AMP-activated protein kinase (AMPK) is positioned to convert changes in cellular Ca^{2+} and energy status into metabolic adaptation. A 2026 CRISPR knock-in study showed that preventing phosphorylation of AMPK α2 at Thr172 diminishes mitochondrial respiration, energy transduction and exercise performance in skeletal muscle (Ryan N. Montalvo et al., 2026). Calcium/calmodulin-dependent protein kinase kinase 2 (CAMKK2) can couple Ca^{2+}-calmodulin signals to AMPK, but this relationship is context-dependent. In proliferating and regenerating myoblasts, CAMKK2-AMPK signalling restrains proliferation and differentiation, cautioning against treating pathway activation as uniformly beneficial (Ye et al., 2016). Zeaxanthin is a dietary xanthophyll carotenoid with reported effects on mitochondrial biogenesis and respiration in adipocytes (Zhao et al., 2021). Whether it protects senescent skeletal muscle by normalizing compartment-specific Ca^{2+} readouts, rather than through a nonspecific antioxidant effect, and whether this response involves CAMKK2-linked AMPK activation remain unresolved.

We addressed this question in a D-galactose-induced accelerated-ageing mouse model and C2-ceramide-induced senescent C2C12 myotubes. The *in vivo* study connected muscle performance and morphology to mitochondrial ultrastructure and markers associated with mitochondrial quality control, whereas the cell model linked organelle-sensitive Ca^{2+} fluorescence and endoplasmic reticulum-mitochondrial colocalization to bioenergetic and myogenic outcomes. Pharmacological experiments with the CaMKK inhibitor STO-609 and the intracellular Ca^{2+} chelator BAPTA-AM tested pathway involvement. Zeaxanthin preserved muscle and mitochondrial architecture *in vivo* and shifted Ca^{2+}, colocalization, respiration, ATP and myogenic readouts in senescent myotubes toward the non-senescent state; these cellular effects accompanied CAMKK2-associated AMPK activation and were attenuated by CaMKK inhibition. The results support a model in which ZEA acts at the interface between compartmental Ca^{2+} homeostasis and mitochondrial quality control. This interpretation is confined to accelerated-ageing and cell-senescence models, steady-state fluorescence and colocalization measurements, and pharmacological evidence for pathway involvement.

2. Materials and Methods

Experimental design

The study combined an *in vivo* D-galactose-induced subacute accelerated skeletal-muscle aging model and *in vitro* C2C12 myotube models of C2-ceramide-induced premature cellular senescence(Azman and Zakaria, 2019). The mouse study was used to assess skeletal-muscle mass, function, histopathology, mitochondrial ultrastructure, oxidative and energetic indices, and AMPK/mitochondrial quality-control signaling. The C2C12 experiments were used to test whether zeaxanthin (ZEA) directly protected

senescent myotubes, whether this effect depended on CAMKK2 signaling, and whether calcium homeostasis contributed to the mitochondrial and myogenic effects.

Zeaxanthin and major reagents

For animal experiments, ZEA with purity ≥ 75% was obtained from Shenzhen Gerui Bo Biotechnology Co., Ltd.; the remaining detected carotenoid component was lutein. ZEA was administered in 0.5% sodium carboxymethylcellulose (CMC-Na). For cell experiments, a 5.0 mM ZEA stock solution was prepared by dissolving 5.0 mg ZEA standard in 1758.5 μL anhydrous DMSO and protecting the solution from light.

C2-ceramide was prepared as a 15.0 mM stock by dissolving 50.0 mg in 976.0 μL ethanol, protected from light and aliquoted. STO-609 was used as the CAMKK2-pathway inhibitor at 30 μM(Tokumitsu et al., 2002). BAPTA-AM was prepared as a 10.0 mM stock in anhydrous DMSO and stored at -80 ℃ protected from light. MitoTracker Green was prepared as a 1.0 mM stock by dissolving 50.0 μg reagent in 74.4 μL anhydrous DMSO and storing at -80 ℃. Mag-Fluo-4 AM was prepared as a 10.0 mM DMSO stock, Rhod-2 AM as a 5.0 mM DMSO stock, and Fluo-3 AM working solution was prepared by 1:2000 dilution in serum-free DMEM.

Animal model and treatment

All animal procedures were approved by the Animal Ethics Committee of Jilin Agricultural University (approval number 2024 02 22 001). Four-week-old male C57BL/6 mice of SPF grade were purchased from Beijing Huafukang Biotechnology Co., Ltd. (license SCXK [Jing] 2019-0008). Mice were housed two per cage at 22 ± 2 ℃ and 50 ± 10% relative humidity with free access to food and water. After a 1-week acclimation period, 48 mice were randomized by an Excel random-number method into four groups (n = 12 per group): control, control + ZEA, D-galactose model, and D-galactose + ZEA.

The intervention lasted 12 weeks. Mice in the ZEA-treated groups received ZEA by gavage at 20 mg/kg/day in 0.5% CMC-Na. Control and model mice received an equal volume of 0.5% CMC-Na. Mice in the D-galactose model and D-galactose + ZEA groups received D-galactose at 250 mg/kg/day by intraperitoneal injection in saline(Xie et al., 2021). Control and control + ZEA mice received an equal volume of saline by intraperitoneal injection.

Body weight, grip endurance and tissue collection

Body weight was recorded weekly. Grip endurance was assessed weekly at a fixed time using an inverted wire-cage hanging test; each mouse was placed on a wire cage cover, the cover was inverted, and the fall latency was recorded in seconds.

At the end of the 12-week intervention, mice were fasted for 12 h, weighed and euthanized. Blood was collected from the orbital sinus and centrifuged at 8200 g for 5 min at -4 ℃ to obtain serum. Liver and kidney tissues were rinsed with cold PBS, weighed for organ-coefficient analysis and stored at -80 ℃. Gastrocnemius (GAS), tibialis anterior (TA) and soleus muscles were dissected bilaterally, weighed and

stored at -80 ℃ unless immediately processed for fixation. The organ coefficients were calculated using the formula: (organ weight / body weight) × 100%. Similarly, the skeletal-muscle wet-weight ratios were calculated as: (skeletal-muscle part weight / body weight) × 100%.

Gastrocnemius HE staining and cross-sectional morphology

Fresh gastrocnemius tissue was fixed in 4% paraformaldehyde for more than 24 h. Tissue blocks were trimmed, dehydrated through graded ethanol, cleared through xylene and embedded in paraffin. The dehydration sequence reported in the source was 75% ethanol for 4 h, 85% ethanol for 2 h, 90% ethanol for 2 h, 95% ethanol for 1 h, absolute ethanol I and II for 30 min each, ethanol/xylene for 5–10 min, xylene I and II for 5–10 min each, and paraffin I-III for 1 h each. Sections were cut at 4 μm, floated on 40 ℃ water to flatten the tissue and baked at 60 ℃.

For HE staining, paraffin sections were deparaffinized through xylene I and II for 20 min each, absolute ethanol I and II for 10 min each, 95%, 90%, 80% and 70% ethanol for 5 min each, and then washed in distilled water. Nuclei were stained with Harris hematoxylin for 3–8 min, differentiated briefly in 1% acid alcohol, blued with 0.6% ammonia water and rinsed. Cytoplasm was stained with eosin for 1–3 min. Sections were dehydrated through 95% ethanol I and II for 5 min each, absolute ethanol I and II for 5 min each, cleared in xylene I and II for 5 min each, mounted with neutral resin, microscopically inspected and imaged. Sections were microscopically inspected and imaged using an upright optical microscope (Nikon Eclipse CI) equipped with an imaging system (Nikon DS-U3, Japan).

Transmission electron microscopy of skeletal muscle

For tissue ultrastructure, gastrocnemius samples were cut along the muscle-fiber direction into approximately 3 × 1 × 1 mm pieces. Samples were fixed overnight in 2.5% glutaraldehyde, rinsed and post-fixed with 1% osmium tetroxide for 1–2 h. Samples were dehydrated through graded ethanol, transferred to pure acetone for 20 min, infiltrated with embedding resin/acetone at 1:1 (v/v) for 1 h and 3:1 (v/v) for 3 h, and then incubated in pure embedding resin overnight at room temperature. Embedded samples were heated at 70 ℃ overnight. Ultrathin sections of 70–90 nm were prepared, stained with lead citrate and uranyl acetate for 5 min each, dried, and imaged by transmission electron microscopy to assess myofibrillar and mitochondrial ultrastructure.

Dystrophin immunofluorescence in gastrocnemius

Paraffin sections were deparaffinized in xylene I and II for 15 min each, absolute ethanol I and II for 5 min each, 85% ethanol for 5 min, 75% ethanol for 5 min, and water. Antigen retrieval was performed in EDTA buffer (pH 9.0) by microwave heating until boiling, followed by intermittent heating for 10 min and cooling. Sections were washed three times in PBS for 5 min each. Primary antibody diluted in PBS was added and sections were incubated overnight at 4 ℃ in a humidified chamber. After PBS washing, a species-matched secondary antibody was added and incubated for 50 min at room temperature in the

dark. Nuclei were counterstained with DAPI for 10 min. Sections were mounted with antifade reagent and imaged using a Nikon Eclipse Ti-SR inverted fluorescence microscope (Nikon, Japan).

Serum and skeletal-muscle biochemical assays

Reactive oxygen species (ROS) content and citrate synthase (CS) activity in serum and skeletal muscle were measured using double-antibody sandwich ELISA kits(Shanghai Enzyme-linked Biotechnology Co). Serum was used after centrifugation. Skeletal-muscle tissue was homogenized in physiological saline under ice-bath conditions, centrifuged, and the supernatant was collected. Samples were stored at -20 ℃ until analysis. Samples and standards were added to pre-coated microplates, incubated with HRP-labelled antibody at 37 ℃ for 60 min, washed, developed with substrate for 15 min and stopped. Absorbance was measured at 450 nm, and concentrations or activities were calculated from standard curves with dilution correction.

Na^+/K^+-ATPase and Ca^{2+}/Mg^{2+}-ATPase activities in skeletal-muscle tissue were measured by colorimetry. Tissue was homogenized with pre-cooled extraction solution at a 1:9 weight-to-volume ratio under ice-bath conditions. Homogenates were centrifuged at 8000 g for 10 min at 4 ℃, and supernatants were kept on ice. Enzymatic reactions were performed at 37 ℃ for 10 min, stopped, centrifuged, developed with phosphate-detection reagent for 30 min and read at 660 nm. Activities were calculated from standard curves and expressed as μmol/h/g fresh weight.

Western blotting of skeletal-muscle tissue

Approximately 25 mg skeletal-muscle tissue was placed into a pre-cooled nuclease-free tube containing 200 μL RIPA lysis buffer, magnetic beads, 2 μL phosphatase inhibitor and 2 μL PMSF/protease inhibitor. The reported RIPA:phosphatase inhibitor:protease inhibitor volume ratio was 100:1:1. Samples were disrupted in a pre-cooled automated tissue/cell grinder under low-temperature intermittent grinding for six cycles of 30 s with 10 s intervals. Homogenates were transferred to new tubes and lysed for 30 min on ice with shaking. Lysates were centrifuged at 12000 g for 5 min at 4 ℃, and supernatants were collected as protein samples.

Protein concentration was determined by BCA assay. BCA reagent and Cu reagent were mixed at 50:1. BSA standards were prepared at 0.5 mg/mL, and 0, 2, 4, 6, 8, 12, 16 or 20 μL standard was added to 96-well plates and brought to 20 μL with PBS. Samples and standards received 200 μL BCA working reagent, were incubated at 37 ℃ for 30 min, and absorbance was measured at 562 nm. Protein lysates were mixed with 5x loading buffer at 4:1 and boiled for 5 min.

For SDS-PAGE, 25 ug protein was loaded per lane and electrophoresed at 150 V until the bromophenol-blue front reached the bottom of the gel. PVDF membranes were activated in methanol for 5–10 s and equilibrated in transfer buffer. Semi-dry transfer was performed for 10 min. Membranes were cut according to target molecular weights and incubated using a SNAP i.d. rapid Western blotting system. Membranes were blocked with 20 mL 5% BSA for 20 min at room temperature. Primary antibodies

diluted in TBST containing 3% BSA were added at 3 mL and incubated for 10 min at room temperature. Membranes were washed four times with 15 mL TBST per incubation slot. Secondary antibody diluted in TBST was added at 3 mL at 1:10000 and incubated for 10 min at room temperature, followed by four TBST washes. ECL reagent was applied for 2–3 min in the dark, chemiluminescent images were acquired, and band intensity was quantified with ImageJ.

GAPDH or β-actin was used as the internal loading control. Primary antibodies and secondary antibodies were obtained from ABclonal Technology Co., Ltd., Affinity Biosciences, and Cell Signaling Technology. Blot quantification was performed based on three independent biological replicates (n = 3).

C2C12 cell culture and differentiation

The C2C12 murine skeletal myoblast cell line was obtained from Saipuno Life Science Co., Ltd. Cells were cultured in growth medium consisting of high-glucose DMEM supplemented with 10% fetal bovine serum and 1% penicillin-streptomycin at 37 ℃ in a humidified incubator with 5% CO_2. Cells were passaged at approximately 80% confluence using trypsin containing 0.02% EDTA, centrifuged at 90 g for 5 min and subcultured at a 1:3 ratio.

For myotube differentiation, cells were seeded into 6-well plates at 9×10^4 cells per well. When cells reached approximately 80% confluence, 2 mL differentiation medium consisting of high-glucose DMEM supplemented with 2% horse serum(Gibco, USA) and 1% penicillin-streptomycin was added to each well. Differentiation medium was changed every 2 days. Cells were differentiated for approximately 6 days until 90–95% myotube formation, depending on the assay module(Kumar et al., 2024).

ZEA cytotoxicity screening and C2-ceramide senescence model

For MTT cell-viability screening, C2C12 cells were seeded in the inner wells of 96-well plates at 3×10^4 cells/mL (with edge wells filled with sterile PBS to prevent evaporation). Cells were serum-starved in DMEM for 12 h and subsequently treated with 0–30 μM ZEA for 12 h, with 3 to 6 technical replicates per condition. To eliminate solvent-induced artifacts, the final vehicle concentration across all treatment and control groups was uniformly adjusted to 0.6% DMSO. Following treatment, MTT reagent (0.5 mg/mL, 100 μL per well) was added, and the plates were incubated for 4 h at 37°C in the dark. Formazan crystals were then dissolved in 100 μL DMSO per well. The plates were shaken for 10 min, and the absorbance was measured at 570 nm using a microplate reader. For the C2-ceramide-induced myotube-senescence model, differentiated C2C12 myotubes were randomly allocated to the control, model, ZEA5, ZEA10, and ZEA15 groups. Control myotubes received 2% horse-serum DMEM containing 0.6% DMSO for 12 h. Model myotubes received 50 μM C2-ceramide in 2% horse-serum DMEM for 12 h. The ZEA groups received 50 μM C2-ceramide plus 5, 10, or 15 μM ZEA in 2% horse-serum DMEM for 12 h. The final vehicle concentration (DMSO) was kept constant across all groups.

Myotube morphology, senescence-associated β-galactosidase and mitochondrial content

For Jenner-Giemsa staining, differentiated myotubes were washed twice with PBS, fixed in methanol for 15 min and air-dried. A working solution of 1 mL Giemsa solution plus 9 mL PBS was prepared, added at 500 μL per well and incubated for 30 min in the dark. Wells were washed with PBS and imaged using a Cytation 10 system. Morphological quantification was performed using ImageJ software (NIH, Bethesda, MD, USA). The fusion index was calculated as the percentage of nuclei residing within multinucleated myotubes relative to the total number of nuclei in five randomly selected fields per well. Myotube diameter was determined by measuring the width at three distinct points along the length of at least 50 randomly selected myotubes per experimental group, and the average was recorded. Senescence-associated β-galactosidase staining was performed after PBS washing. Cells were fixed with 1 mL β-galactosidase fixative for 15 min at room temperature, washed three times with PBS and incubated overnight at 37 ℃ with 1 mL working solution consisting of 1 μL solution A, 10 μL solution B, 50 μL X-Gal and 930 μL solution C. Images were acquired with a Cytation 10 system. The intensity of the blue senescence signal was quantified using the color deconvolution plugin in ImageJ, and the total integrated density was subsequently normalized to the total protein content determined by the BCA assay.Mitochondrial content was assessed using MitoTracker Green. Stock solution was diluted 1:20000 in serum-free DMEM. Cells received 1 mL working solution per well for 10 min at 37 ℃ in the dark. Hoechst 33342 was added at a final 1× concentration for 3–5 min at room temperature in the dark. Images were acquired with Cytation 10, and relative fluorescence was measured. Fluorescence segmentation and quantification were performed in ImageJ by applying a fixed global threshold to delineate MitoTracker-positive regions. The mean fluorescence intensity (MFI) of the segmented mitochondrial network was calculated and normalized to the corresponding number of Hoechst-stained nuclei in each field.

CAMKK2 inhibition experiments

For CAMKK2-pathway inhibition, differentiated C2C12 myotubes were assigned to control, model, ZEA, STO and STO + ZEA groups. Control cells received 2% horse-serum DMEM for 12 h. Model cells received 50 μM C2-ceramide for 12 h. ZEA cells received 50 μM C2-ceramide plus 15 μM ZEA for 12 h. STO cells were pretreated with the CAMKK2 inhibitor STO-609 at 30 μM for 2 h, washed twice with PBS and then treated with 50 μM C2-ceramide for 12 h. STO + ZEA cells were pretreated with 30 μM STO-609 for 2 h, washed twice with PBS and then treated with 50 μM C2-ceramide plus 15 μM ZEA for 12 h.

Cellular ROS, ATP and oxygen-consumption measurements

Intracellular oxidant-sensitive DCF fluorescence was assessed using DCFH-DA. DCFH-DA was diluted 1:1000 in serum-free medium to 10 μM. After 12 h drug treatment, cells were washed three times with PBS, incubated with 1 mL DCFH-DA working solution per well for 20 min at 37 ℃ and washed three times with serum-free medium. Images were acquired using Cytation 10, fluorescence was measured with a plate reader and values were normalized to protein content.

ATP was measured after 12 h drug treatment using an ATP detection kit. Cells in 6-well plates were washed three times with PBS and lysed with 200 μL lysis buffer per well. Plates were shaken on ice for

15 min, and lysates were centrifuged at 900 g for 5 min at 4 ℃. ATP working solution (100 μL per detection well) was equilibrated for 5 min, 20 μL diluted sample was added, relative luminescence units were measured and ATP concentration was calculated from a standard curve.

Oxygen-consumption rate (OCR) was measured with a Seahorse XFp analyzer. C2C12 cells were seeded on Seahorse XF/XFp assay plates at 6×10^3 cells per well in 80 μL medium, allowed to settle for 1 h and cultured overnight. Cells were differentiated in 200 μL 2% horse-serum DMEM, with medium changed every 2 days for approximately 6 days until about 95% myotube formation. The probe plate was hydrated the day before analysis. Assay medium consisted of 17 mL Seahorse XF DMEM, 1 mL glucose, 1 mL pyruvate and 1 mL glutamine and was equilibrated at 37 ℃ without CO2 for 1 h(Murphy et al., 2022). Oligomycin, FCCP and rotenone/antimycin A working solutions were loaded into the assay cartridge ports according to the source protocol, and OCR parameters including basal respiration, ATP-linked respiration, maximal respiration and spare respiratory capacity were analyzed(Divakaruni et al., 2014).

Calcium chelation, mitochondrial membrane potential and calcium-probe imaging

For calcium-chelation experiments, differentiated C2C12 myotubes were assigned to control, model, ZEA and BAP groups. Control cells received 2% horse-serum DMEM for 12 h. Model cells received 50 μM C2-ceramide for 12 h. ZEA cells received 50 μM C2-ceramide plus 15 μM ZEA for 12 h. BAP cells were pretreated with 10 μM BAPTA-AM for 2 h, washed twice with PBS and then treated with 50 μM C2-ceramide plus 15 μM ZEA in 2% horse-serum DMEM for 12 h.

Mitochondrial membrane potential was assessed with JC-1. Cells were washed twice with PBS, incubated with a 1:1 mixture of culture medium and JC-1 working solution at 2 mL per well for 20 min at 37 ℃ in the dark, washed twice with JC-1 buffer and returned to 2 mL medium. Images were acquired with Cytation C10, and the red/green fluorescence ratio was calculated.

Mitochondrial Ca^{2+} was measured with Rhod-2 AM diluted 1:1000 in pre-warmed HBSS. Cells received 1 mL per well for 45 min at 37 ℃ in the dark, were washed twice with HBSS and returned to 1 mL medium. Images were acquired with Cytation 10. For fluorescence measurement, cell suspensions were added at 100 μL per well with four replicate wells, read at excitation 549 nm/emission 578 nm and normalized to BCA protein content.

Cytosolic Ca^{2+} was measured with Fluo-3 AM diluted 1:2000 in serum-free DMEM. Cells received 1 mL per well for 30 min at 37 ℃ in the dark, were washed three times with serum-free medium and incubated for another 30 min in 1 mL medium. Images were acquired with Cytation 10. Cell suspensions were read at 100 μL per well with four replicate wells at excitation 506 nm/emission 526 nm and normalized to protein content.

Endoplasmic-reticulum Ca^{2+} was measured with Mag-Fluo-4 AM diluted 1:2000 in pre-warmed HBSS. Cells received 1 mL per well for 30 min at 37 ℃ in the dark, were washed twice and returned to 1 mL

medium. Images were acquired with Cytation C10. Cell suspensions were read at 100 µL per well with four replicate wells at excitation 475 nm/emission 515 nm and normalized to protein content.

Mitochondria-ER colocalization and cell TEM

Mitochondria-ER colocalization was assessed using MitoTracker Green and ER-Tracker Red. MitoTracker Green was diluted 1:20000 in serum-free DMEM and added at 1 mL per well for 10 min at 37 ℃ in the dark. Cells were washed once with PBS and incubated with ER-Tracker Red diluted 1:2000 at 1 mL per well for 20 min at 37 ℃ in the dark. Hoechst 33342 was added at a final 1x concentration for 3–5 min at room temperature in the dark. Cells were washed three times with PBS and imaged using Cytation C10. Pearson and Mander colocalization coefficients were calculated(Aaron et al., 2018).

For cell TEM, cells were scraped at low temperature and centrifuged at 180 g for 10 min. Cell pellets were fixed overnight in 2.5% glutaraldehyde, dehydrated through an acetone gradient, infiltrated with resin, cut into 60–80 nm ultrathin sections, stained with uranyl acetate and lead citrate, and imaged by transmission electron microscopy.

Western blotting of C2C12 cells

For cell protein extraction, cells were lysed with RIPA-based lysis buffer containing protease and phosphatase inhibitors at a ratio of 1 mL RIPA, 10 µL protease inhibitor and 10 µL phosphatase inhibitor. Protein concentration was measured by BCA assay at 562 nm. Proteins were loaded at 25 µg per lane. PVDF membranes were activated in methanol for 5–10 s, and transfer was performed at 2.5 A for 10 min per gel. Membranes were blocked with 20 mL 5% BSA for 20 min. Primary antibody solution (3 mL; dilution according to the manufacturer) was incubated for 10 min using a Western blot accelerator, followed by four TBST washes. Secondary antibody (3 mL, 1:2000) was incubated for 10 min at room temperature, followed by four TBST washes. Bands were developed with ECL, images were captured using a chemiluminescence system and grayscale intensity was quantified using ImageJ.

RT-qPCR

Total RNA was extracted from C2C12 cells, washed with 1 mL pre-cooled 75% ethanol prepared in DEPC-treated water and centrifuged at 900 g for 5 min at 4 ℃. RNA pellets were air-dried for approximately 5 min, dissolved in 50–100 µL RNA dissolution solution, mixed by pipetting and incubated at 60 ℃ for 10 min. RNA concentration and purity were measured by micro-ultraviolet spectrophotometry, and samples with OD260/OD280 between 1.8 and 2.0 were used or stored at -80 ℃.The primer design is shown in Table S1.

Reverse transcription was performed in RNase-free PCR tubes on a 4 ℃ metal bath according to the source kit system, with RNA input adjusted according to RNA concentration. cDNA was stored at -80 ℃ before use. qPCR was performed in 20 µL reactions containing 10 µL 2× Universal SYBR Green Fast qPCR Mix, variable cDNA template, 0.4 µL forward primer (10 µM), 0.4 µL reverse primer (10 µM) and ultrapure water to 20 µL. The cDNA volume did not exceed one-tenth of the total qPCR reaction volume.

β-actin was used as the internal control, and relative expression was calculated using the $2^{-\Delta\Delta Ct}$ method(Livak and Schmittgen, 2001).

Statistical analysis

All data are expressed as the mean ± standard deviation (SD). For *in vitro* C2C12 cell assays, experiments were performed in at least three independent biological replicates (n ≥ 3). Statistical analyses and data visualization were performed using GraphPad Prism software (versions 9.0 and 9.5). Prior to parametric analysis, the normality of data distribution was evaluated using the Shapiro-Wilk test, and homogeneity of variance was confirmed using the Brown-Forsythe test. Comparisons among multiple groups were evaluated using a one-way analysis of variance (ANOVA). Following ANOVA, Duncan's multiple-comparison test (for animal studies) and Tukey's post hoc test (for cell studies) were applied to assess differences between specific groups. No data points or statistical outliers were excluded from the final analyses. A *p*-value of < 0.05 was considered statistically significant.

3. Results and Conclusion

3.1 Protective Effects of Zeaxanthin on Sarcolemmal Framework and Myofibrillar Architecture During Aging

To evaluate the impact of zeaxanthin (ZEA) on sarcolemmal integrity during D-galactose (D-gal)-induced muscle aging, we examined the expression and localization of dystrophin, a pivotal scaffold protein essential for bridging the actin cytoskeleton to the extracellular matrix and maintaining muscle membrane stability. Immunofluorescence analysis revealed that the Control (Con) and Con + ZEA groups exhibited robust, continuous peripheral ring-like dystrophin staining tightly delineated along the sarcolemma (Fig. 1A). Conversely, chronic D-gal administration induced a disruption of the sarcolemmal dystrophin network, manifested as fragmented, discontinuous, and attenuated fluorescent signals (Fig. 1A). Quantitative evaluation confirmed a statistically significant reduction in the relative fluorescence intensity within the D-gal group, which dropped to 77.7% of the control baseline ($p < 0.05$; Fig. 1B), indicating extensive membrane destabilization and potential myofiber vulnerability. ZEA supplementation counteracted this senescent decline, rescuing the dystrophin immunofluorescence intensity to 113% of the D-gal model cohort ($p < 0.05$; Fig. 1B), thereby demonstrating its efficacy in safeguarding the structural framework of the sarcolemma against age-associated degradation.

To further elucidate the protective efficacy of ZEA at the subcellular level, transmission electron microscopy (TEM) was employed to resolve the myofibrillar ultramicrostructure of the gastrocnemius muscle (Fig. 1C). Myofibrils in the Con and Con + ZEA cohorts displayed a highly ordered, tightly packed sarcomeric architecture, characterized by distinct alternating light (I) bands and dark (A) bands, bisected by sharp, well-defined Z-lines and M-lines. In stark contrast, the D-gal-induced aging mice exhibited ultrastructural alterations. This pathological degeneration was typified by the chaotic misalignment of myofibrils, the near-complete obliteration of I-bands, Z-lines, and M-lines, and a loose, disordered

dispersion of thick and thin myofilaments. Notably, intervention with ZEA effectively mitigated these senescent lesions, largely restoring the parallel alignment of myofibrils and successfully reconstituting the definition of the sarcomeric band-and-line architecture. Taken together, these findings demonstrate that ZEA exerts a potent protective effect against senescent skeletal muscle atrophy by sustaining sarcolemmal protein networks and preserving myofibrillar structural homeostasis(Belhasan and Akaaboune, 2020).

3.2 Zeaxanthin Rejuvenates Mitochondrial Quality Control and Activates the AMPK Signaling Axis in Senescent Skeletal Muscle

To investigate whether ZEA prevents age-dependent mitochondrial deterioration in skeletal muscle, TEM was performed to evaluate mitochondrial ultrastructure. In the Control and Con + ZEA groups, mitochondria exhibited normal elliptical profiles with densely packed, well-defined cristae and intact outer membranes. Conversely, chronic D-galactose (D-gal) exposure precipitated profound mitochondrial damage, manifested as irregular swelling(Guan et al., 2025), structural deformation, widespread cristae disruption, and clear vacuolization (Fig. 2A). Strikingly, ZEA intervention substantially alleviated these pathological abnormalities, preserving membrane integrity and partially restoring cristae architecture.

To elucidate the molecular mechanisms underlying this structural preservation, the expression profiles of key proteins governing mitochondrial dynamics and mitophagy were examined by Western blotting. The levels of the mitochondrial fusion proteins mitofusin-2 (MFN2) and optic atrophy 1 (OPA1) were significantly suppressed in the D-gal group compared to the controls, but were rescued upon ZEA treatment ($p < 0.05$, Fig. 2B). Concurrently, the mitophagy pathway—critical for the clearance of damaged mitochondria—was evaluated(Leduc-Gaudet et al., 2021). Chronically aged mice exhibited a pronounced downregulation of PTEN-induced kinase 1 (PINK1) and the autophagosome marker microtubule-associated protein 1 light chain 3-II (LC3-II), coupled with an accumulation of the autophagic substrate P62, indicating a blockade in mitophagy flux. ZEA supplementation effectively reversed these alterations, significantly upregulating PINK1 and LC3-II protein levels while facilitating the degradation of P62 ($p < 0.05$, Fig. 2B). These findings indicate that ZEA maintains mitochondrial quality control by driving both mitochondrial fusion and mitophagy.

Given that the adenosine monophosphate-activated protein kinase (AMPK) cascade serves as a master energy sensor regulating mitochondrial biogenesis and antioxidant defenses, we assessed its activation status(Guo and Lu, 2024). Chronic D-gal exposure markedly suppressed AMPK phosphorylation (p-AMPK/AMPK) and downregulated its downstream effectors, including PGC1-α, Nrf2, TFAM, and HO-1. ZEA administration significantly enhanced AMPK phosphorylation and upregulated the protein expression levels of PGC1-α, Nrf2, TFAM, and HO-1 ($p < 0.05$, Fig. 2C). Collectively, these data demonstrate that ZEA protects against senescent skeletal muscle atrophy by activating the AMPK/PGC1-α/Nrf2 signaling axis, thereby comprehensively restoring mitochondrial quality control and metabolic homeostasis.

3.3 Zeaxanthin Attenuates C2-Ceramide-Induced Myotube Atrophy and Cellular Senescence by Preserving Mitochondrial Mass and Myogenic Capacity

To characterize the cytoprotective efficacy of zeaxanthin (ZEA) against age-associated skeletal muscle wasting, we evaluated the morphologic differentiation and phenotypic senescence of C2C12 myotubes using an established C2-ceramide-induced cellular model(Jadhav et al., 2013). Jenner-Giemsa staining revealed that while the Control group developed dense, elongated, and highly multinucleated myotube networks, MOD group induced structural alterations, typified by a reduction in total myotube density and the prominent shrinkage of cells into isolated spherical aggregates (Fig. 3A). This morphologic deterioration was directly accompanied by a profound induction of cellular senescence, as visualized by an accumulation of deep blue cytochemical products via SA-β-gal staining (Fig. 3B) (Gorgoulis et al., 2019). Quantitative optical density profiling confirmed that SA-β-gal enzymatic activity increased significantly in the MOD cohort compared to the Control baseline ($p < 0.0001$, Fig. 3B). Intervention with ZEA at progressive doses (5, 10, and 15 μM) successfully countered these degenerative changes in a clear concentration-dependent manner. ZEA supplementation significantly preserved myotube width and longitudinal continuity while decreasing SA-β-gal expression levels to 0.78-fold, 0.70-fold, and 0.68-fold of the MOD group values, respectively (Fig. 3B), thereby substantiating its capacity to impede ceramide-driven replicative senescence.To establish a non-cytotoxic concentration range, we assessed C2C12 myoblast viability following treatment with 5–30 μM zeaxanthin using an MTT assay. Zeaxanthin at 5–15 μM did not significantly affect cell viability, whereas concentrations of 20 μM or higher reduced viability (Figure S1). We therefore used 5–15 μM zeaxanthin in subsequent experiments.

To uncover the downstream transcriptional and translational mechanisms governing this structural rejuvenation, the expression patterns of critical myogenic regulatory factors and catabolic ubiquitin E3 ligase pathway components were systematically profiled (Fig. 3C). Real-time quantitative PCR (RT-qPCR) analyses demonstrated that senescent injury in the MOD group led to a substantial suppression of the essential muscle differentiation transcripts MYOD and MYH1(Bodine et al., 2001), which fell by 0.47-fold and 0.64-fold relative to controls, alongside a parallel upregulation of the atrophic markers FOXO-3a (1.39-fold) and MURF-1 (1.17-fold). High-dose ZEA administration (ZEA15) reversed this pathological transcriptional profile, elevating MYOD and MYH1 mRNA expression by 1.38-fold and 1.60-fold, respectively, while effectively downregulating FOXO-3a and MURF-1 transcripts by 0.47-fold and 0.46-fold compared to the untreated senescent model (Fig. 3C). Western blot analysis validated that these transcriptomic modulations correlated with protein expression dynamics. ZEA15 treatment significantly rescued the translation of MYOD and MYH1 proteins ($p < 0.01$) while downregulating the intracellular protein abundance of the catabolic drivers MURF-1 and FOXO-3a ($p < 0.05$, Fig. 3C). This dual modulation indicates that ZEA preserves myotube dimensions by simultaneously suppressing ubiquitin-proteasome-mediated proteolysis and reactivating the endogenous myogenic repair program(Shirakawa et al., 2022).

Given that the maintenance of skeletal muscle mass is fundamentally linked to metabolic energy efficiency and organelle integrity, we next quantified alterations in mitochondrial content using MitoTracker Green fluorescent probing (Fig. 3D). Senescent C2C12 cells within the MOD cohort exhibited an explicit, severe loss of green fluorescence intensity compared to the Control group ($p < 0.0001$), demonstrating extensive mitochondrial depletion during myoblast aging. Consistent with the morphological improvements, ZEA replenishment achieved a dose-dependent restoration of the functional mitochondrial network. Specifically, the relative fluorescence intensity in the ZEA15 cohort was markedly elevated relative to the MOD baseline ($p < 0.001$, Fig. 3D) (Belhasan and Akaaboune, 2020; Wu et al., 2025). These cytochemical findings clarify that the therapeutic efficacy of ZEA in mitigating senescent myotube atrophy is intimately coupled with its capacity to halt mitochondrial quantitative decline and reinforce sub-cellular structural homeostasis(Larsson et al., 2019).

3.4 Zeaxanthin Restores Subcellular Calcium Homeostasis and Preserves Mitochondrial-Endoplasmic Reticulum Interfacial Dynamics in Senescent myotubes

To evaluate whether ZEA alleviates senescent muscle degradation by modulating inter-organelle calcium crosstalk, we systematically quantified compartmentalized Ca^{2+} flux across the ER, cytoplasm, and mitochondria using cell-permeable fluorescent indicators (Fig. 4A). In the MOD group, a profound destabilization of the intracellular calcium reservoir was observed, characterized by a substantial evacuation of Ca^{2+} from the ER lumen, which subsequently triggered a pathological elevation of calcium concentrations within the cytoplasm and the mitochondrial matrix ($p < 0.0001$, Fig. 4A). Intracellular calcium chelation via BAPTA-AM (BAP group) efficiently arrested this abnormal effluence, verifying the dependency of mitochondrial calcium overload on aberrant ER release(Barazzuol et al., 2021). Remarkably, ZEA supplementation fundamentally stabilized this tripartite calcium network; under ZEA intervention, luminal ER Ca^{2+} levels were maintained at 1.11-fold of the MOD cohort, while cytosolic and intramitochondrial Ca^{2+} accumulations were significantly suppressed to 0.84-fold and 0.87-fold of the senescent baseline, respectively ($p < 0.05$, Fig. 4A). This restoration of sub-cellular ion homeostasis directly correlated with the preservation of mitochondrial membrane potential ($\Delta\psi_m$), as evidenced by JC-1 ratiometric imaging (Fig. 4B). While the MOD group underwent extensive mitochondrial depolarization, ZEA treatment effectively prevented this bioenergetic collapse, achieving a significant 1.32-fold increase in the JC-1 red-to-green fluorescence ratio relative to the untreated model group ($p < 0.05$, Fig. 4B).

Given that excessive mitochondrial calcium accumulation often arises from abnormal physical apposition between the ER and outer mitochondrial membranes, we next examined the structural configuration of mitochondria-associated endoplasmic reticulum membranes (MAMs) via dual-fluorescence colocalization of MitoTracker Green and ER-Tracker Red (Fig. 4C). Quantitative morphological profiling revealed that senescent stress significantly intensified the structural packing and number of MAM junctions, driven by a sharp elevation in both the Pearson colocalization coefficient

(0.767 ± 0.027) and Mander's overlap coefficient (0.795 ± 0.093) relative to healthy controls ($p < 0.001$, Fig. 4C). ZEA intervention effectively disrupted this pathological inter-organelle tethering, successfully reducing the Pearson and Mander's coefficients to 0.663 ± 0.016 and 0.633 ± 0.008, respectively ($p < 0.05$, Fig. 4C). At the translational level, Western blot analysis demonstrated that ZEA significantly repressed the senescent overexpression of core calcium-channel components localized within these contact sites, downregulating the IP3R and MCU to 0.74-fold and 0.75-fold of the MOD level, while concurrently rescuing the expression of the crucial outer and inner mitochondrial fusion proteins MFN2 and OPA1 ($p < 0.05$, Fig. 4D) (Filadi and Pizzo, 2019). These macromolecular modulations were validated by TEM microstructural analysis (Fig. 4F). The distinct mitochondrial swelling, cristae dissolution, vacuolization, and cisternal ER fragmentation characteristic of the MOD group were markedly attenuated in the ZEA and BAP cohorts, which retained substantially integrated cristae architectures and intact reticular networks.

To determine how the stabilization of interfacial calcium transport impacts long-term mitochondrial quality control, we analyzed downstream markers regulating organelle biogenesis, gatekeeping, and autophagic clearance (Fig. 4E). Western blotting indicated that ZEA profoundly upregulated the inner membrane calcium-sensing gateway proteins MICU1 and MICU2, thereby reconstructing the threshold mechanism necessary to shield the matrix from toxic calcium spikes ($p < 0.05$, Fig. 4E). Concurrently, ZEA promoted transcription-coupled organelle renewal by elevating the expression of the PGC-1α and TFAM to 1.23-fold and 1.72-fold of the MOD baseline, respectively ($p < 0.05$, Fig. 4E). Furthermore, ZEA effectively enhanced mitophagy flux to clear compromised structures, stimulating the accumulation of the PINK and the LC3-II to 1.25-fold and 1.14-fold of the model levels ($p < 0.05$, Fig. 4E).

3.5 Zeaxanthin Drives Mitochondrial Bioenergetic Recovery and Myogenic Differentiation via a Calcium-Dependent CAMKK2/AMPK Metabolic Signaling Axis

To establish the molecular dependency of ZEA-mediated mitochondrial protection on upstream energetic signaling networks, we monitored the activation of the CAMKK2 cascade and downstream metabolic homeostatic regulators following pharmacological challenge with the selective inhibitor STO-609. RT-qPCR and Western blot profiling demonstrated that C2-ceramide-induced senescent injury in the MOD group severely repressed the transcription and phosphorylation of the CAMKK2 axis and its classical downstream nuclear effectors, including CREB and transducer of regulated CREB activity (TORC) (Fig. 5A). ZEA replenishment robustly reversed these senescent deficits, expanding the transcript numbers of CAMKK2, CREB, and TORC by 3.04-, 2.13-, and 3.20-fold relative to the MOD group, respectively, while substantially promoting their corresponding protein phosphorylation levels ($p < 0.05$, Fig. 5A). This up-regulatory efficacy was comprehensively abolished upon STO-609 administration, with the CAMKK2, CREB, and TORC transcripts in the STO + ZEA cohort dropping to 0.69-, 0.76-, and 0.40-fold of the ZEA group baseline, respectively (Fig. 5A). Parallel signaling blockades were observed within the downstream AMPK energy-sensing loop. ZEA-mediated transcriptomic upregulation of AMPK (1.87-fold), ACC (1.78-fold), and SIRT1 (1.88-fold) over the MOD group—along with their corresponding protein

phosphorylation points—was effectively blunted under STO-609 co-treatment (Fig. 5B). These findings confirm that ZEA dictates downstream nutrient-sensing and enzymatic network remodeling through the direct activation of the upstream CAMKK2 signaling axis.

To determine how this CAMKK2-dependent signaling cascade governs mitochondrial physiological output, we quantified cellular reactive oxygen species (ROS) accumulation, real-time oxygen consumption rates (OCR), and total adenylate charge generation. The MOD cohort exhibited extensive oxidative stress, manifesting as a sharp elevation in DCFH-DA-mediated green fluorescence intensity ($p < 0.0001$, Fig. 5C). ZEA intervention efficiently quenched this oxidative burden, depressing intracellular ROS levels to 0.40-fold of the MOD cohort, whereas CAMKK2 inhibition via STO-609 induced a distinct 1.83-fold elevation in ROS accumulation within the STO + ZEA group compared to ZEA alone ($p < 0.0001$, Fig. 5C). This metabolic dependency was further verified by cellular bioenergetic flux analysis (Fig. 5D). While senescent myoblasts underwent profound respiratory collapse, ZEA treatment restored fundamental mitochondrial parameters, significantly boosting basal respiration, maximal respiration, ATP-linked oxygen consumption, and spare respiratory capacity ($p < 0.05$, Fig. 5D). Total intracellular ATP chemical analysis supported these kinetic findings, showing that ZEA elevated ATP production to 1.74-fold of the untreated senescent level, a therapeutic enhancement that was negated when upstream CAMKK2 activity was pharmacologically blocked (Fig. 5E). Taken together, these data demonstrate that ZEA-driven bioenergetic restoration and oxidative stress mitigation are fundamentally dependent on intact CAMKK2 enzymatic function.

To resolve the upstream physiological trigger initiating this CAMKK2 signaling loop, we tracked intracellular calcium dynamics and long-term myogenic commitment following organelle-targeted calcium chelation with BAPTA-AM. Ratiometric JC-1 fluorometric tracking across a multi-hour screening timeline confirmed that a 2 h exposure period optimized the recovery of mitochondrial membrane potential ($\Delta\psi_m$), effectively establishing the operational conditions for evaluating calcium-dependent signaling restoration (Fig. 5F). Quantitative bioenergetic profiling indicated that sustaining cellular calcium homeostasis directly augmented total ATP synthesis, with the ZEA and BAP cohorts increasing ATP generation to 1.45-fold and 2.00-fold of the senescent MOD baseline, respectively ($p < 0.05$, Fig. 5G). Crucially, this calcium stabilization retroactively driven the phosphorylation-dependent activation of the CAMKK2 enzyme itself, raising P-CAMKK2 abundance to 1.17-fold (ZEA) and 1.41-fold (BAP) of the model group values ($p < 0.05$, Fig. 5H). This ion-dependent signaling correction ultimately determined downstream structural preservation within the contractile apparatus (Fig. 5I). Western blot analysis confirmed that both ZEA and BAP interventions significantly suppressed the translation of the prominent muscle-wasting E3 ubiquitin ligases FOXO-3a (0.91-fold and 0.85-fold of MOD) and MURF-1 (0.84-fold and 0.77-fold of MOD). Concurrently, this stabilization reactivated the expression of the essential terminal myogenic differentiation proteins MYOD (1.29-fold and 1.50-fold of MOD) and MYH1 (1.32-fold and 1.55-fold of MOD) ($p < 0.05$, Fig. 5I). Collectively, these experimental results elucidate a clear homeostatic mechanism whereby ZEA regulates intracellular calcium architecture to activate the CAMKK2 metabolic pathway, thereby suppressing muscle-wasting proteolysis and preserving the structural commitment of skeletal myotubes.

4. Discussion

Sarcopenia is characterized by progressive impairment of muscle mass, structure and function, yet effective pharmacological or nutritional interventions remain limited. In the present study, ZEA attenuated sarcopenia-like changes in D-gal-treated mice and C2-ceramide-induced senescent C2C12 myotubes. *In vivo*, ZEA preserved dystrophin organization, myofibrillar architecture and mitochondrial ultrastructure, while shifting markers of mitochondrial fusion, autophagy-related quality control and AMPK-associated signalling towards the control state. In senescent myotubes, ZEA improved myotube morphology, reduced senescence-associated β-galactosidase activity, increased MitoTracker signal, and improved mitochondrial membrane potential, oxygen consumption and ATP production. Based on the results of this study, it can be inferred that in preclinical aging-related models, ZEA protects skeletal muscle by coordinating its effects on muscle fiber integrity, mitochondrial homeostasis, and intracellular calcium ion handling.

The *in vivo* findings suggest that preservation of muscle architecture and mitochondrial quality control are closely linked in the D-gal model. Dystrophin disruption and myofibrillar disorganization indicate compromised sarcolemmal and contractile integrity, whereas swollen mitochondria with disrupted cristae indicate impaired energy-generating capacity. ZEA improved both features and restored MFN2, OPA1, PINK1, LC3-II and p62 in directions consistent with improved mitochondrial fusion and autophagy-related quality control. Although these static protein measurements do not directly establish mitophagic flux, their concordance with the ultrastructural findings supports a model in which ZEA limits the accumulation of damaged mitochondria in senescent skeletal muscle. Similar improvements in muscle morphology, mitochondrial regulation and atrophy-associated signalling have been reported for other nutritional interventions in D-gal-induced models, including krill oil and danshensu sodium salt (Lim et al., 2025)(Wu et al., 2026). Our findings extend this work by placing intracellular Ca^{2+} compartmentalization and ER-mitochondria interactions upstream of the mitochondrial phenotype.

A central observation in senescent myotubes was the redistribution of Ca^{2+} across intracellular compartments. C2-ceramide exposure was associated with lower ER Ca^{2+} signal and increased cytosolic and mitochondrial Ca^{2+} signals, together with higher ER-mitochondria colocalization. ZEA shifted these measurements toward the control state, preserving ER Ca^{2+} signal while reducing cytosolic and mitochondrial Ca^{2+} accumulation. Because ER-mitochondria interfaces coordinate local Ca^{2+} transfer and metabolic communication, this pattern is consistent with the possibility that ZEA limits chronic ER-to-mitochondria Ca^{2+} transfer under senescent stress. Similarly, colocalization supports altered ER-mitochondria association but does not by itself quantify physical MAM number, distance or transfer activity. Thus, the data support MAM remodelling as a plausible component of the ZEA response, rather than demonstrating direct regulation of MAM structure.

This interpretation should also be considered in light of the context-dependent nature of Ca^{2+} dysregulation in ageing muscle. Natural ageing can be associated with reduced mitochondrial proximity

to Ca^{2+} release units and impaired activity-evoked mitochondrial Ca^{2+} uptake (Gherardi et al., 2025). Conversely, altered MAM composition, Ca^{2+} imbalance and disturbed organelle dynamics have also been described in ageing striated muscle (Lu et al., 2022)(Allen et al., 2025). These observations are not necessarily contradictory. Reduced transient Ca^{2+} uptake during contraction and excessive chronic Ca^{2+} transfer from the ER may arise in different ageing contexts, cell states or disease stages. Our C2-ceramide model appears to reflect the latter condition, in which sustained ER-mitochondria association is accompanied by mitochondrial Ca^{2+} accumulation and bioenergetic impairment. ZEA may therefore act by restoring the distribution of Ca^{2+} among intracellular compartments rather than by uniformly increasing or suppressing mitochondrial Ca^{2+} uptake. This framework is also compatible with the reported effects of Polygonatum sibiricum polysaccharide on MAM-associated Ca^{2+} homeostasis in ageing muscle models (Chen et al., 2024).

The functional mitochondrial data provide an important link between Ca^{2+} redistribution and protection of myotube integrity. ZEA reduced oxidant-sensitive fluorescence and improved mitochondrial membrane potential, basal respiration, maximal respiration, ATP-linked respiration, spare respiratory capacity and ATP content in senescent myotubes. These changes were accompanied by recovery of myogenic markers and reduced expression of FoxO3a and MuRF1. Thus, restoration of mitochondrial bioenergetics may help sustain the anabolic capacity of senescent myotubes while limiting activation of atrophy-associated programmes. The BAPTA-AM plus ZEA experiments further support the involvement of intracellular Ca^{2+} homeostasis in this response, because Ca^{2+} chelation under the tested conditions was associated with improved mitochondrial and myogenic readouts.

Our results also associate ZEA-mediated mitochondrial recovery with CAMKK2/AMPK signalling. ZEA increased CAMKK2-, CREB-, TORC- and AMPK-related readouts in senescent myotubes, whereas STO-609 attenuated these ZEA-associated signalling and bioenergetic effects. AMPK α2 activation is important for skeletal-muscle energy transduction and mitochondrial respiration, providing a biologically credible connection between the observed signalling changes and mitochondrial recovery (Ryan N Montalvo et al., 2026). In adult skeletal muscle, genetic and selective-inhibitor studies have indicated that CAMKK2 is dispensable for contraction-stimulated AMPK activation and that STO-609 can exert off-target effects (Negoita et al., 2023). The distinct cellular context of C2-ceramide-induced senescence may explain why CAMKK2-associated signalling is responsive here, but this possibility requires validation using genetic loss-of-function approaches and additional selective inhibitors.

Several limitations define the scope of this study. First, D-gal-treated mice and C2-ceramide-induced senescent C2C12 myotubes model selected features of ageing-related muscle degeneration but do not reproduce natural ageing or human sarcopenia. Second, the Ca^{2+} and ER-mitochondria measurements were obtained using steady-state fluorescent probes and colocalization analyses; live Ca^{2+} flux measurements, quantitative ultrastructural assessment of ER-mitochondria contact distance and targeted analysis of MAM proteins are needed to test the proposed sequence of events. Finally, the CAMKK2/AMPK interpretation is based principally on STO-609 sensitivity and should be tested using

genetic CAMKK2 and AMPK α2 perturbation. Finally, the ZEA preparation had a purity of at least 75% and contained residual lutein, so the contribution of individual carotenoids should be resolved using chemically defined preparations, pharmacokinetic studies and dose-response experiments.

In conclusion, the present findings identify ZEA as a candidate nutritional modulator of sarcopenia-like muscle degeneration in preclinical models. The data support a model in which ZEA is associated with restoration of intracellular Ca^{2+} partitioning, reduced pathological ER-mitochondria colocalization, improved mitochondrial bioenergetics and preservation of myogenic capacity. Future work in naturally aged animals, human-relevant systems and genetic models will determine whether regulation of Ca^{2+}-MAM-mitochondrial signalling can be developed into a reproducible therapeutic strategy for age-related muscle dysfunction.

5. Conclusion

Together, these findings identify ZEA as a protective modulator of sarcopenia-like muscle atrophy in accelerated aging and cellular senescence models. In D-galactose-treated mice, ZEA preserved sarcolemmal dystrophin organization, myofibrillar architecture and mitochondrial ultrastructure, while restoring markers linked to mitochondrial fusion, mitophagy and AMPK-associated mitochondrial quality-control signaling. In C2-ceramide-induced C2C12 myotubes, ZEA reduced senescence-associated β-galactosidase activity, maintained myotube morphology, restored mitochondrial content and bioenergetic output, and shifted myogenic and atrophy-related markers toward a less degenerative state. Mechanistically, the cellular data support a model in which ZEA stabilizes intracellular Ca^{2+} homeostasis, limits pathological ER-mitochondrial coupling and mitochondrial Ca^{2+} overload, and couples these effects to CAMKK2/AMPK-dependent metabolic recovery. The loss of ZEA-mediated signaling and bioenergetic benefits after CAMKK2 inhibition further indicates that this pathway is required for full mitochondrial protection in senescent myotubes. These conclusions remain bounded by the preclinical systems tested here: a D-galactose-induced mouse model and a C2-ceramide-induced C2C12 myotube model, rather than natural aging or human sarcopenia.

Declarations

Author Contribution

Tianyu Liu: Methodology; Validation; Formal analysis; Investigation; Writing-original draft; Visualization. Zhina Hao: Investigation; Formal analysis; Writing-review & editing. Yuan Chen: Investigation; Formal analysis. Wanying Li: Investigation; Formal analysis. Chunlei Liu：Conceptualization. Xiuying Xu： Validation. Jingsheng Liu: Validation; Formal analysis. Meihong Liu: Conceptualization; Writing-review & editing; Supervision; Project administration. Guangquan Ren：Writing-review & editing; Project administration.

Acknowledgment

This work was supported by the National Natural Science Foundation of China (No.32201955), and National Key Research and Development Program of China (2025YFD2100403-1), and the earmarked fund for the China Agriculture Research System (CARS-02).

References

1. Aaron, J., Taylor, A., Chew, T.-L., 2018. Image co-localization – co-occurrence versus correlation. J. Cell Sci. 131, jcs211847. https://doi.org/10.1242/jcs.211847
2. Allen, R.J., Kronemberger, A., Shi, Q., Pope, M., Cuadra-Muñoz, E., Son, W., Song, L.-S., Anderson, E.J., Pereira, R.O., Lira, V.A., 2025. Altered relaxation and mitochondria-endoplasmic reticulum contacts precede major (mal)adaptations in aging skeletal muscle and are prevented by exercise. https://doi.org/10.1101/2025.01.14.633043
3. Azman, K.F., Zakaria, R., 2019. d-galactose-induced accelerated aging model: an overview. Biogerontology 20, 763–782. https://doi.org/10.1007/s10522-019-09837-y
4. Barazzuol, L., Giamogante, F., Calì, T., 2021. Mitochondria associated membranes (MAMs): architecture and physiopathological role. Cell Calcium 94, 102343. https://doi.org/10.1016/j.ceca.2020.102343
5. Belhasan, D.C., Akaaboune, M., 2020. The role of the dystrophin glycoprotein complex on the neuromuscular system. Neurosci. Lett. 722, 134833. https://doi.org/10.1016/j.neulet.2020.134833
6. Bodine, S.C., Latres, E., Baumhueter, S., Lai, V.K.-M., Nunez, L., Clarke, B.A., Poueymirou, W.T., Panaro, F.J., Na, E., Dharmarajan, K., Pan, Z.-Q., Valenzuela, D.M., DeChiara, T.M., Stitt, T.N., Yancopoulos, G.D., Glass, D.J., 2001. Identification of ubiquitin ligases required for skeletal muscle atrophy. Science 294, 1704–1708. https://doi.org/10.1126/science.1065874
7. Chen, Wenhao, Shen, Z., Dong, W., Huang, G., Yu, D., Chen, Weizhe, Yan, X., Yu, Z., 2024. Polygonatum sibiricum polysaccharide ameliorates skeletal muscle aging via mitochondria-associated membrane-mediated calcium homeostasis regulation. Phytomedicine 129, 155567. https://doi.org/10.1016/j.phymed.2024.155567
8. Divakaruni, A.S., Paradyse, A., Ferrick, D.A., Murphy, A.N., Jastroch, M., 2014. Chapter sixteen - analysis and interpretation of microplate-based oxygen consumption and pH data, in: Murphy, A.N., Chan, D.C. (Eds.), Mitochondrial Function, Methods in Enzymology. Academic Press, pp. 309–354. https://doi.org/10.1016/B978-0-12-801415-8.00016-3
9. Filadi, R., Pizzo, P., 2019. ER-mitochondria tethering and Ca2 + crosstalk: the IP3R team takes the field. Cell Calcium 84, 102101. https://doi.org/10.1016/j.ceca.2019.102101
10. Gherardi, G., Weiser, A., Bermont, F., Migliavacca, E., Brinon, B., Jacot, G.E., Hermant, A., Sturlese, M., Nogara, L., Vascon, F., De Mario, A., Mattarei, A., Garratt, E., Burton, M., Lillycrop, K., Godfrey, K.M., Cendron, L., Barron, D., Moro, S., Blaauw, B., Rizzuto, R., Feige, J.N., Mammucari, C., De Marchi, U., 2025b. Mitochondrial calcium uptake declines during aging and is directly activated by oleuropein to

boost energy metabolism and skeletal muscle performance. Cell Metab. 37, 477–495.e11. https://doi.org/10.1016/j.cmet.2024.10.021

11. Gorgoulis, V., Adams, P.D., Alimonti, A., Bennett, D.C., Bischof, O., Bishop, C., Campisi, J., Collado, M., Evangelou, K., Ferbeyre, G., Gil, J., Hara, E., Krizhanovsky, V., Jurk, D., Maier, A.B., Narita, M., Niedernhofer, L., Passos, J.F., Robbins, P.D., Schmitt, C.A., Sedivy, J., Vougas, K., von Zglinicki, T., Zhou, D., Serrano, M., Demaria, M., 2019. Cellular senescence: defining a path forward. Cell 179, 813–827. https://doi.org/10.1016/j.cell.2019.10.005
12. Guan, K., Liu, X., Lu, W., Mao, Yuhao, Mao, Yirong, Ma, Y., Wang, R., Li, Q., 2025. Bioactive milk-derived nutrient MFG-E8 ameliorates skeletal muscle atrophy induced by mitochondria damage in aging rats via activating the MAPK/ERK signaling pathway. J. Dairy Sci. 108, 1182–1197. https://doi.org/10.3168/jds.2024-25532
13. Guo, K., Lu, Y., 2024. Acupuncture modulates the AMPK/PGC-1 signaling pathway to facilitate mitochondrial biogenesis and neural recovery in ischemic stroke rats. Front. Mol. Neurosci. 17. https://doi.org/10.3389/fnmol.2024.1388759
14. Jadhav, K.S., Dungan, C.M., Williamson, D.L., 2013. Metformin limits ceramide-induced senescence in C2C12 myoblasts. Mech. Ageing Dev. 134, 548–559. https://doi.org/10.1016/j.mad.2013.11.002
15. Janssens, G.E., Trętowicz, M.M., Grevendonk, L., Kotte, M., Scantlebery, A., Schomakers, B.V., van Weeghel, M., Hermans, J., Vervaart, M.A.T., Wever, E.J.M., Denis, S.W., Jongejan, A., Salomons, G.S., Vaz, F.M., Schrauwen, P., Hoeks, J., Houtkooper, R.H., 2026. Delayed molecular aging, preservation of energy metabolism and enhanced exercise response in exercise-trained human muscle. Nat. Aging 1–19. https://doi.org/10.1038/s43587-026-01150-x
16. Kumar, A., Bellar, A., Mishra, S., Sekar, J., Welch, N., Dasarathy, S., 2024. L-isoleucine reverses hyperammonemia-induced myotube mitochondrial dysfunction and post-mitotic senescence. J. Nutr. Biochem. 123, 109498. https://doi.org/10.1016/j.jnutbio.2023.109498
17. Larsson, L., Degens, H., Li, M., Salviati, L., Lee, Y. il, Thompson, W., Kirkland, J.L., Sandri, M., 2019. Sarcopenia: aging-related loss of muscle mass and function. Physiol. Rev. 99, 427–511. https://doi.org/10.1152/physrev.00061.2017
18. Leduc-Gaudet, J.-P., Hussain, S.N.A., Barreiro, E., Gouspillou, G., 2021. Mitochondrial dynamics and mitophagy in skeletal muscle health and aging. Int. J. Mol. Sci. 22, 8179. https://doi.org/10.3390/ijms22158179
19. Lim, P., Woo, S.W., Han, J., Lee, Y.L., Shim, J.H., Kim, H.S., 2025. Danshensu sodium salt alleviates muscle atrophy via CaMKII - PGC1α - FoxO3a signaling pathway in D-galactose-induced models. FASEB J. 39, e70280. https://doi.org/10.1096/fj.202402158R
20. Livak, K.J., Schmittgen, T.D., 2001. Analysis of relative gene expression data using real-time quantitative PCR and the 2-ΔΔCT method. Methods 25, 402–408. https://doi.org/10.1006/meth.2001.1262
21. Lu, X., Gong, Y., Hu, W., Mao, Y., Wang, T., Sun, Z., Su, X., Fu, G., Wang, Y., Lai, D., 2022. Ultrastructural and proteomic profiling of mitochondria-associated endoplasmic reticulum membranes reveal aging

signatures in striated muscle. Cell Death Dis. 13, 296–310. https://doi.org/10.1038/s41419-022-04746-4

22. Montalvo, Ryan N., Li, X., Many, G.M., Sagendorf, T.J., Yu, Q., Shen, W., Wase, N., Burgardt, A.R., Zhang, T., Gritsenko, M.A., Gaffrey, M.J., Bhonsle, H., Guan, Y., Mao, X., Zhang, M., Qian, W.-J., Yan, Z., 2026. Ampk alpha2 T172 activation dictates exercise performance and energy transduction in skeletal muscle. Sci. Adv. 12, eaeb3338. https://doi.org/10.1126/sciadv.aeb3338
23. Murphy, M.P., Bayir, H., Belousov, V., Chang, C.J., Davies, K.J.A., Davies, M.J., Dick, T.P., Finkel, T., Forman, H.J., Janssen-Heininger, Y., Gems, D., Kagan, V.E., Kalyanaraman, B., Larsson, N.-G., Milne, G.L., Nyström, T., Poulsen, H.E., Radi, R., Van Remmen, H., Schumacker, P.T., Thornalley, P.J., Toyokuni, S., Winterbourn, C.C., Yin, H., Halliwell, B., 2022. Guidelines for measuring reactive oxygen species and oxidative damage in cells and in vivo. Nat. Metab. 4, 651–662. https://doi.org/10.1038/s42255-022-00591-z
24. Negoita, F., Addinsall, A.B., Hellberg, K., Bringas, C.F., Hafen, P.S., Sermersheim, T.J., Agerholm, M., Lewis, C.T.A., Ahwazi, D., Ling, N.X.Y., Larsen, J.K., Deshmukh, A.S., Hossain, M.A., Oakhill, J.S., Ochala, J., Brault, J.J., Sankar, U., Drewry, D.H., Scott, J.W., Witczak, C.A., Sakamoto, K., 2023. CaMKK2 is not involved in contraction-stimulated AMPK activation and glucose uptake in skeletal muscle. Mol. Metab. 75, 101761. https://doi.org/10.1016/j.molmet.2023.101761
25. Pietrangelo, L., D'Incecco, A., Ainbinder, A., Michelucci, A., Kern, H., Dirksen, R.T., Boncompagni, S., Protasi, F., 2015. Age-dependent uncoupling of mitochondria from Ca^{2+} release units in skeletal muscle. Oncotarget 6, 35358–35371. https://doi.org/10.18632/oncotarget.6139
26. Santiago-Fernández, O., Coletto, L., Tasset, I., Kaushik, S., Concepcion, A.R., Qaisar, R., Macho-González, A., Lindenau, K., Diaz, A., Khawaja, R.R., Donega, S., Banskota, N., Ubaida-Mohien, C., Pharaoh, G., Ahn, B., Hartnell, L.M., Ramírez-Pardo, I., Chavda, B., Gazteluiturri, A., Kinter, M., Ferrucci, L., Reisz, J.A., D'Alessandro, A., Van Remmen, H., Muñoz-Cánoves, P., Feske, S., Cuervo, A.M., 2025. Age-related decline of chaperone-mediated autophagy in skeletal muscle leads to progressive myopathy. Nat. Metab. 7, 2589–2611. https://doi.org/10.1038/s42255-025-01412-9
27. Shi, R., Zhang, Y., Chen, G., Zhang, J., Liu, J., Zhu, H., Sun, M., Duan, Y., 2026. Ageing-dependent thyroid hormone receptor α reduction activates IP3R1-meditated Ca^{2+} transfer in MAM and exacerbates skeletal muscle atrophy in mice. Cell Prolif. 59, e70120. https://doi.org/10.1111/cpr.70120
28. Shirakawa, T., Toyono, T., Inoue, A., Matsubara, T., Kawamoto, T., Kokabu, S., 2022. Factors regulating or regulated by myogenic regulatory factors in skeletal muscle stem cells. Cells 11, 1493. https://doi.org/10.3390/cells11091493
29. Tokumitsu, H., Inuzuka, H., Ishikawa, Y., Ikeda, M., Saji, I., Kobayashi, R., 2002. STO-609, a specific inhibitor of the Ca2+/calmodulin-dependent protein kinase kinase*. J. Biol. Chem. 277, 15813–15818. https://doi.org/10.1074/jbc.M201075200
30. Wu, C., Tong, Y., Huang, J., Wang, S., Kobori, H., Zhang, Z., Suzuki, K., 2025. Atrophic C2C12 myotubes activate inflammatory response of macrophages in vitro. Cells 14, 317.

https://doi.org/10.3390/cells14050317

31. Wu, Z.-J., Zhao, X.-Y., Yang, Y.-H., Wang, C.-C., Zheng, Y., Wu, S.-X., Yang, C.-Y., Wei, H.-N., Zou, Q.-Y., Wang, Y.-M., Du, L., 2026. Krill oil attenuates skeletal muscle atrophy during D-galactose-induced accelerated aging via an AMPK-dependent mechanism. Npj Sci. Food 1–18. https://doi.org/10.1038/s41538-026-01081-2
32. Xie, W., He, M., Yu, D., Wu, Y., Wang, X., Lv, S., Xiao, W., Li, Y., 2021. Mouse models of sarcopenia: classification and evaluation. J. Cachexia Sarcopenia Muscle 12, 538–554. https://doi.org/10.1002/jcsm.12709
33. Ye, C., Zhang, D., Zhao, L., Li, Y., Yao, X., Wang, H., Zhang, S., Liu, W., Cao, H., Yu, S., Wang, Y., Jiang, J., Wang, H., Li, X., Ying, H., 2016. CaMKK2 suppresses muscle regeneration through the inhibition of myoblast proliferation and differentiation. Int. J. Mol. Sci. 17, 1695. https://doi.org/10.3390/ijms17101695
34. Zhao, B., Liu, M., Liu, H., Xie, J., Yan, J., Hou, X., Liu, J., 2021. Zeaxanthin promotes browning by enhancing mitochondrial biogenesis through the PKA pathway in 3T3-L1 adipocytes. Food Funct. 12, 6283–6293. https://doi.org/10.1039/d1fo00524c

Figures

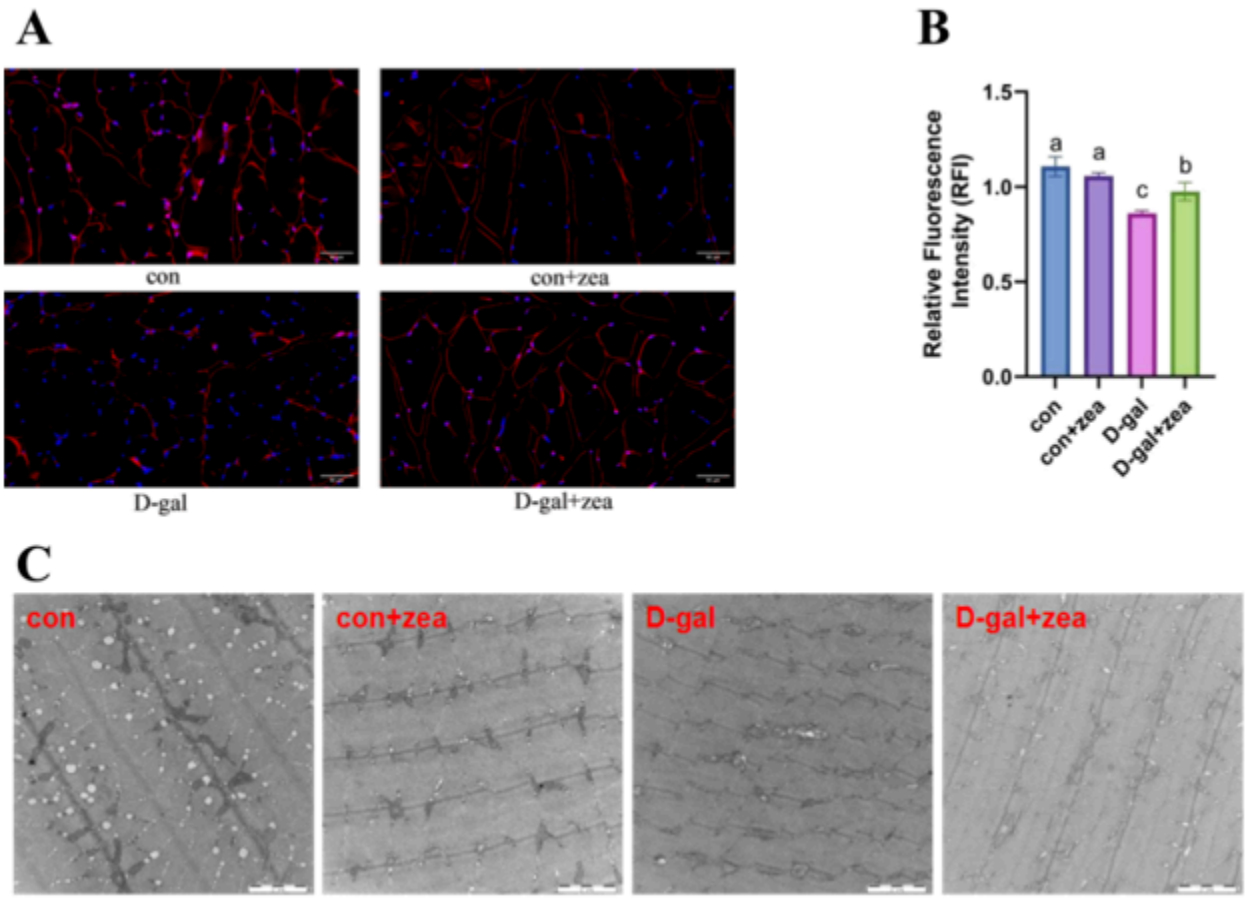


Figure 1

Zeaxanthin alleviates D-galactose-induced skeletal muscle atrophy and structural damage in mice.

(A) Representative immunofluorescence staining of dystrophin (red) in the transverse sections of mouse gastrocnemius muscle from the Control (Con), Con + ZEA, D-galactose (D-gal), and D-gal + ZEA groups (scale bar = 50 μm).

(B) Quantitative analysis of the relative fluorescence intensity of dystrophin across different experimental groups. Data are presented as mean ± standard deviation (SD) (n = 3). Columns with different lowercase letters indicate statistically significant differences ($p < 0.05$) determined by one-way ANOVA followed by Tukey's post hoc test.

(C) Transmission electron microscopy (TEM) micrographs revealing the ultra-microstructure of mouse gastrocnemius muscle fibers (scale bar = 2 μm)

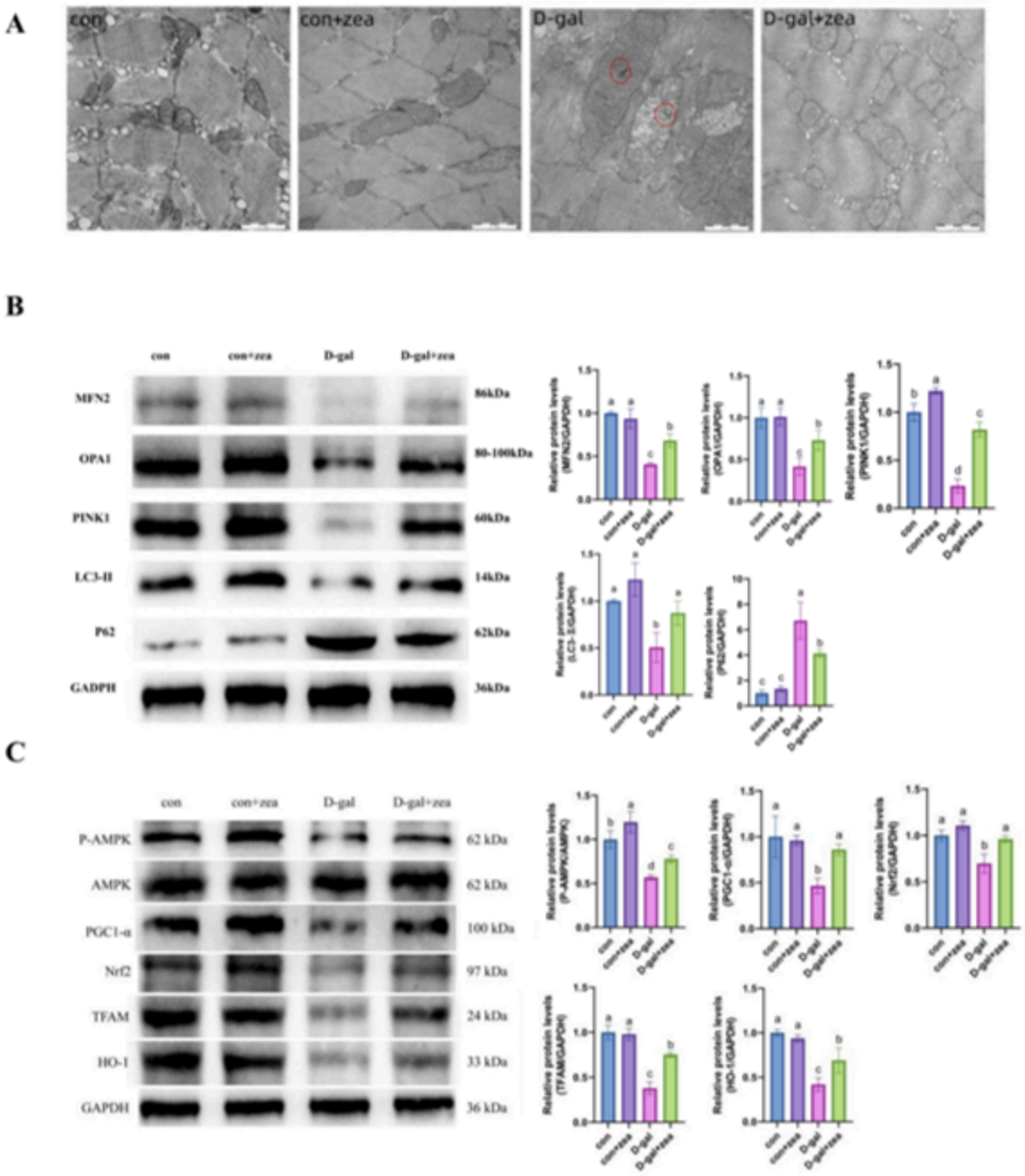


Figure 2

Effects of zeaxanthin on mitochondrial ultrastructure and autophagy-related proteins in the skeletal muscle of D-gal-induced aging mice.

(A) Transmission electron microscopy (TEM) observation of mitochondrial morphology in mouse skeletal muscle (scale bar = 1 μm). Red circles indicate damaged mitochondria with disrupted cristae or vacuolization.

(B, C) Western blot analysis and quantification of PINK1, LC3-II, P62, and p-AMPK protein levels in skeletal muscle. Data are presented as mean ± SD (n = 3). Different letters (a, b, c, d) indicate statistically

significant differences ($p < 0.05$). The relative protein expression levels of PINK1, LC3-II, and P62 were normalized to GAPDH. The phosphorylation level of AMPK (p-AMPK) was normalized to total AMPK.

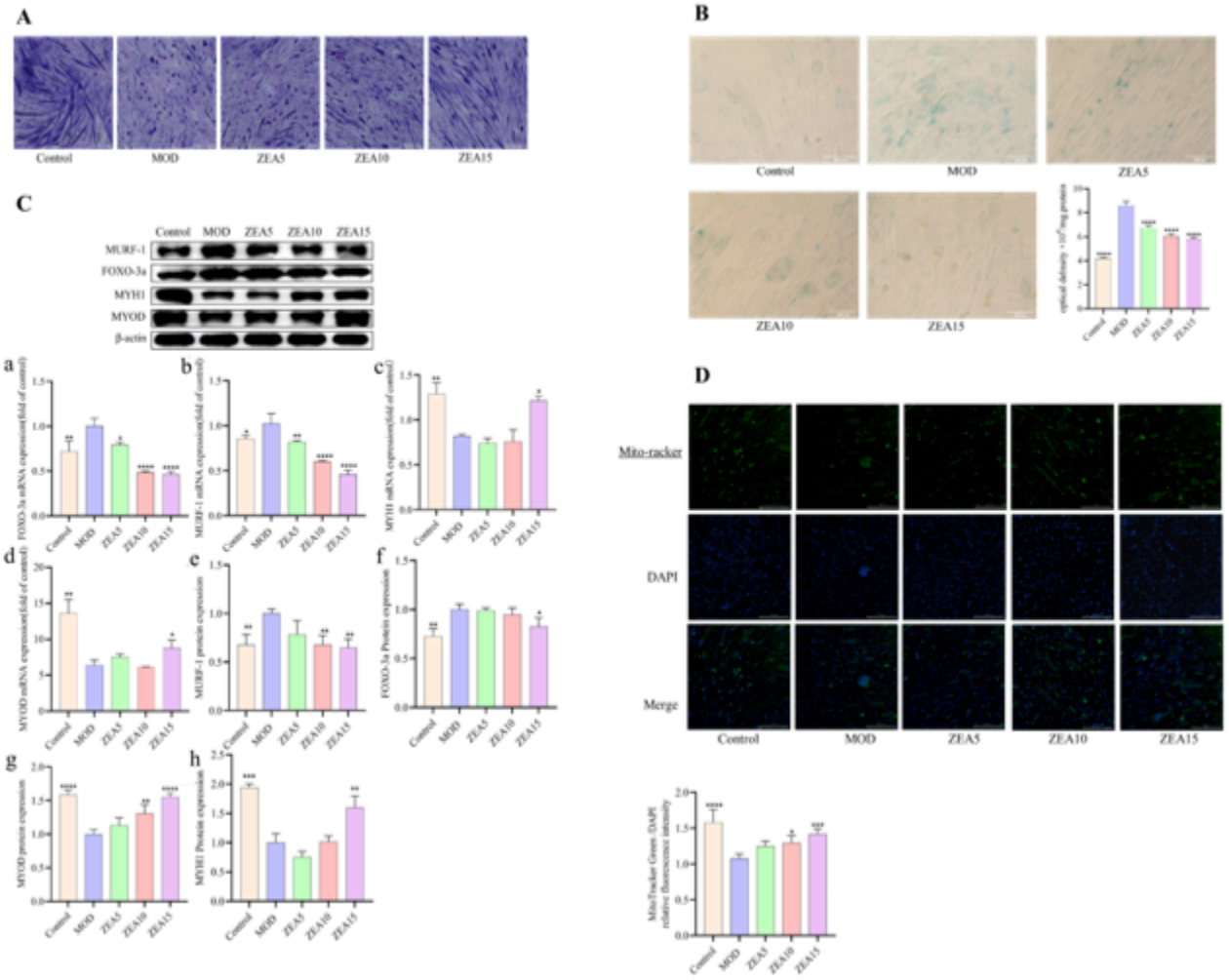


Figure 3

Zeaxanthin suppresses cellular senescence and muscle atrophy while promoting myogenesis in C2C12 myoblasts.

(A) Representative light microscopy images of Jenner-Giemsa staining showing myotube differentiation and morphological changes.

(B) Representative images of senescence-associated beta-galactosidase (SA-β-gal) staining and relative quantification of β-galactosidase activity.

(C) Western blot analysis and RT-qPCR quantification of myogenesis factors (MYOD and MYH1) and muscle atrophy factors (FOXO-3a and MURF-1) at both mRNA and protein levels.

(D) Representative images of MitoTracker Green fluorescent probing and relative quantification of mitochondrial fluorescence intensity to evaluate mitochondrial mass.

Note:Data are presented as mean ± SD (n = 3). Statistically significant differences are indicated as *p < 0.05, p < 0.01, ***p < 0.001, and ****p < 0.0001.

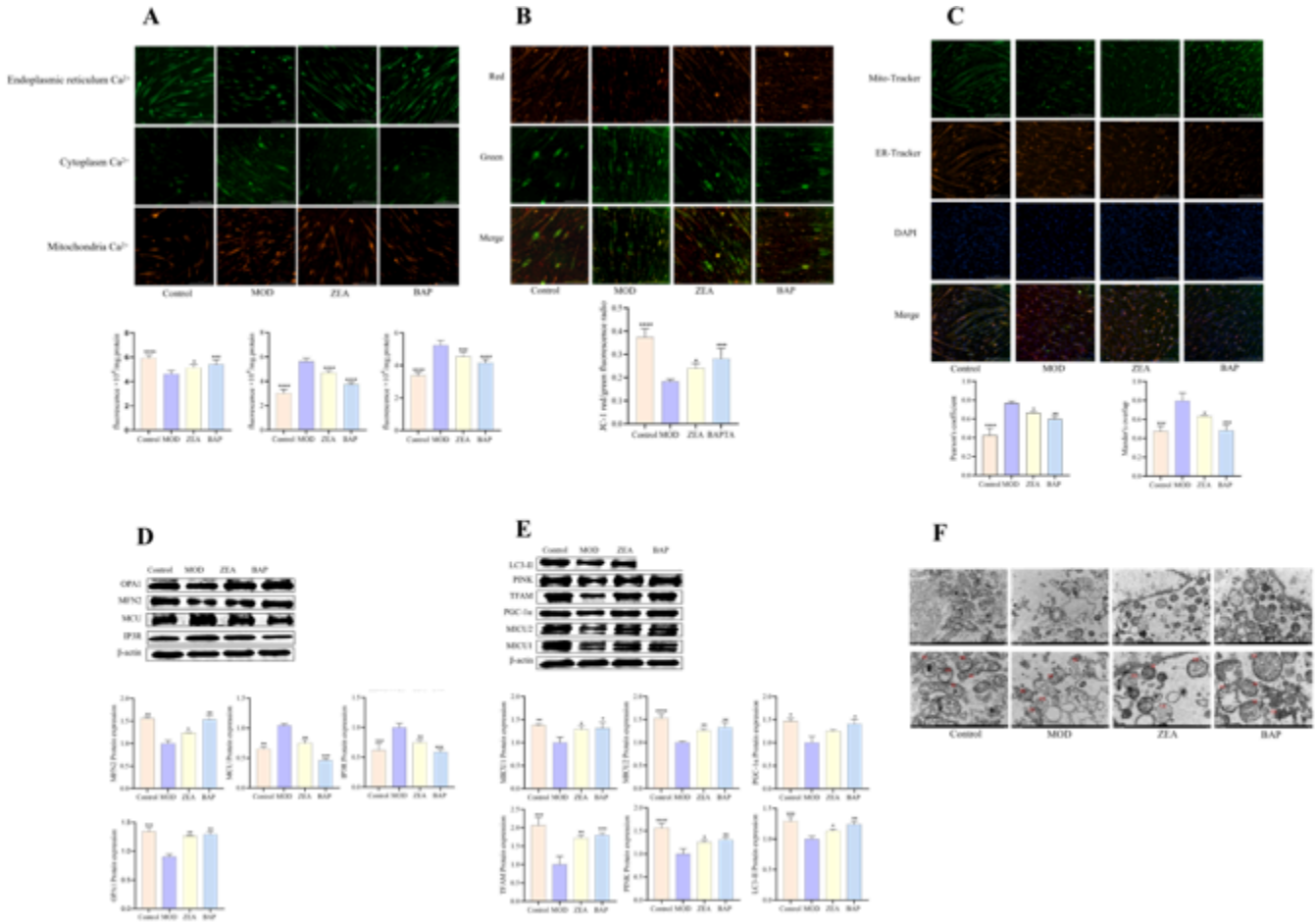


Figure 4

Zeaxanthin improves mitochondrial function and mitochondria-associated endoplasmic reticulum membranes (MAMs) in senescent skeletal muscle (C2C12) cells by regulating Ca^{2+} homeostasis.

(A) Characterization of Ca^{2+} levels in the endoplasmic reticulum, cytoplasm, and mitochondria of C2C12 cells. The distribution of Ca^{2+} in different subcellular regions was detected using specific fluorescent probes (Mag-Fluo-4 AM, Fluo-3 AM, and Rhod-2 AM), accompanied by the quantitative analysis of relative fluorescence intensity for each group (Scale bar = 200 μm).

(B) Alterations of mitochondrial membrane potential (MMP) in senescent C2C12 cells. Representative confocal fluorescence images (Red/Green/Merge) of cells stained with the JC-1 probe, and the quantitative statistical analysis of the JC-1 red-to-green fluorescence intensity ratio used to indicate changes in MMP (Scale bar = 200 μm).

(C) Colocalization analysis of mitochondria-associated endoplasmic reticulum membranes (MAMs). Representative images of multi-color immunofluorescence staining using MitoTracker (green, indicating mitochondria), ER-Tracker (red, indicating endoplasmic reticulum), and DAPI (blue, indicating nuclei). The statistical graphs of Pearson's correlation coefficient and Mander's overlap coefficient are provided to evaluate the degree of colocalization between mitochondria and the endoplasmic reticulum (Scale bar = 200 μm).

(D) Expression levels of proteins related to mitochondrial fusion and calcium channels. Representative Western blot images and quantitative analysis of mitochondrial fusion proteins (OPA1, MFN2), mitochondrial inner membrane calcium channel protein (MCU), and the MAM-resident calcium channel constituent protein (IP3R).

(E) Expression levels of mitochondrial homeostasis marker proteins. Western blot images and corresponding quantitative analysis showing the expression of key mitophagy proteins (LC3-II, PINK), mitochondrial biogenesis marker proteins (TFAM, PGC-1α), and key Ca^{2+} transport proteins (MICU2, MICU1).

(F) Transmission electron microscopy (TEM) images of the mitochondria-endoplasmic reticulum structure. Representative TEM images showing ultrastructural morphological alterations of mitochondria (e.g., swelling, loss/disruption of cristae) and the endoplasmic reticulum in each group. Red arrows indicate specific structural abnormalities (Magnification A: 1:10,000; Magnification B: 1:20,000).

Note: In all panels, Control refers to the normal culture group; MOD refers to the cell senescence model group induced by 50 μM C2-ceramide; ZEA refers to the 15 μM zeaxanthin intervention group; BAP refers to the group treated with the intracellular calcium chelator BAPTA-AM. Data are presented as mean ± standard deviation (SD) of three independent experiments (n=3). Statistical significance is denoted as follows compared with the MOD group: *$p < 0.05$, $p < 0.01$, ***$p < 0.001$, ****$p < 0.0001$. β-actin was used as an internal loading control for protein quantification.

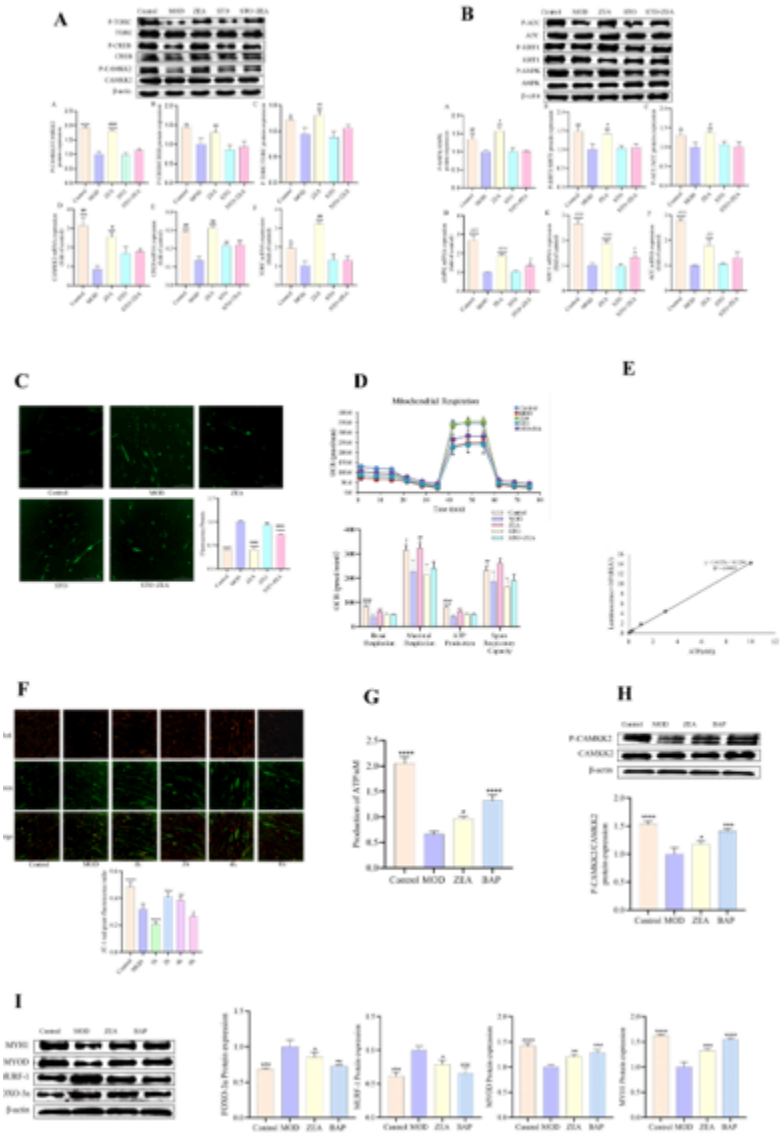


Figure 5

Note: Control represents the normal culture group; MOD represents the C2-ceramide-induced senescence model group; ZEA represents the zeaxanthin intervention group. In the pathway inhibition experiments (A-E), STO represents the STO-609 (CAMKK2 inhibitor) group, and STO+ZEA represents the combined STO-609 and zeaxanthin group. In the calcium homeostasis experiments (F-I), BAP represents the BAPTA-AM (Ca^{2+} chelator) pretreatment followed by zeaxanthin intervention group. Data are expressed as mean ± standard deviation (SD) of three independent experiments (n=3). Statistical significance compared to the MOD group is denoted as *p < 0.05, p < 0.01, ***p < 0.001, and ****p < 0.0001; significance compared to the STO group is denoted as #p < 0.05, ##p < 0.01, ###p < 0.001, and ####p < 0.0001. β-actin was used as an internal control for protein normalization.

Zeaxanthin enhances mitochondrial energy metabolism and myogenic ability in senescent C2C12 cells via the CAMKK2 signaling pathway and intracellular Ca^{2+} homeostasis.

(A-E) Validation of the CAMKK2 pathway and mitochondrial function (STO-609 intervention):

(A) Expression levels of CAMKK2 pathway-related factors. Representative Western blots and quantitative analysis of mRNA and protein phosphorylation levels for CAMKK2, CREB, and TORC in each group.

(B) Expression levels of energy metabolism-related factors. Representative Western blots and quantitative analysis of mRNA and protein phosphorylation levels for AMPK, SIRT1, and ACC.

(C) Intracellular reactive oxygen species (ROS) production. Representative ROS fluorescence images and the corresponding quantitative relative fluorescence intensity (Scale bar = 200 μm).

(D) Mitochondrial respiration capacity. Oxygen consumption rate (OCR) traces measured by the Seahorse XFp analyzer, along with quantitative bar charts for basal respiration, maximal respiration, ATP production, and spare respiratory capacity.

(E) ATP production levels. Quantitative analysis of ATP production under CAMKK2 pathway inhibition, accompanied by the standard curve for ATP measurement.

(F-I) Validation of Ca^{2+} homeostasis and myogenic phenotype (BAPTA-AM intervention):

(F) Screening of the optimal BAPTA-AM action time. Representative confocal images of JC-1 staining and quantitative analysis of the red/green fluorescence ratio to evaluate mitochondrial membrane potential (MMP) recovery at different time points (Scale bar = 200 μm).

(G) ATP production based on Ca^{2+} homeostasis. Quantitative analysis of cellular ATP production following intracellular Ca^{2+} chelation.

(H) Activation of the CAMKK2 pathway. Representative Western blot and quantitative analysis of P-CAMKK2/CAMKK2 expression, demonstrating the regulatory effect of Ca^{2+} homeostasis on the CAMKK2 pathway.

(I) Expression levels of myogenic and muscle atrophy-related proteins. Representative Western blots and quantitative analysis of myogenic factors (MYH1, MYOD) and muscle atrophy factors (MURF-1, FOXO-3a).

Supplementary Files

This is a list of supplementary files associated with this preprint. Click to download.

- file.docx
- WBsupplementarydocument.pdf